Rare Met. (2023) 42(12):4153–4166
https://doi.org/10.1007/s12598-023-02344-7

RARE METALS

ORIGINAL ARTICLE

Interface engineering of $ZnSnO_3$-based heterojunctions for room-temperature methanol monitoring

Jin-Yong Xu, Kai-Chun Xu, Xiao-Xi He, Han-Lin Liao, Marc Debliquy, Qiao-Quan Liu, Chao Zhang*

Received: 16 January 2023 / Revised: 21 February 2023 / Accepted: 25 February 2023 / Published online: 25 October 2023

Abstract Detecting methanol is of great importance in the organic synthesis industry. Herein, the effective utilization of $ZnSnO_3$-based microstructures for room-temperature methanol monitoring was realized through a template-free approach. $ZnSnO_3$-based heterojunctions with different structures and morphologies were successfully synthesized via regulating the molar ratio of Zn^{2+} and Sn^{4+} sources. And room-temperature sensing properties towards methanol were investigated. Among them, ZnO/$ZnSnO_3$ hollow microcubes exhibited an outstanding sensing performance including a high sensitivity (10.16) and a response/recovery time (14/75 s) and a limit of detection (490×10^{-9}) towards 5×10^{-6} methanol. Additionally, the synergistic effects of hollow structure with larger specific surface areas (42.277 $m^2 \cdot g^{-1}$), the construction of n–n heterojunctions formed at $ZnSnO_3$ and ZnO interfaces, the high percentage of dissociative and chemisorbed oxygen are the main causes of the elevated sensing characteristics. Besides, the practical experiment demonstrated that ZnO/$ZnSnO_3$ was capable of on-field monitoring methanol in the chemical reaction utilizing H_2 and CO_2 as raw materials. Moreover, with the help of density functional theory calculations, the enhanced sensing properties of ZnO/$ZnSnO_3$ are due to the special tuning effects of Zn ionic sites on methanol adsorption.

Keywords $ZnSnO_3$; Heterojunctions; Methanol; Gas sensor; Density functional theory calculations

1 Introduction

Over the last few decades, the rapid development of global industry-embedded lifestyle has inevitably contributed to serious environmental pollution, especially hazardous gas emissions from various sources. Currently, considering the toxic components and their harmful effects on human health, reliable and accurate gas monitoring equipment is under intense investigation. Among those toxic gases, volatile organic compounds (VOCs) (i.e., methanol, ethanol, isopropanol) are essential indicators of health hazards [1, 2]. As a common hazardous gas, methanol has been extensively detected in industrial production. The residual trace of methanol in the reaction will enter the environment with the discharge of wastewater, which may cause harm to environmental water bodies and/or organisms [3, 4]. Accordingly, it is urgent need to real-time monitor and identify the variation of methanol in our surrounding environment. Up to now, various instrumental analysis techniques, such as near-infrared spectroscopy [5], liquid gas chromatography-mass spectrometry [6] and

Supplementary Information The online version contains supplementary material available at https://doi.org/10.1007/s12598-023-02344-7.

J.-Y. Xu, K.-C. Xu, X.-X. He, C. Zhang*
College of Mechanical Engineering, Yangzhou University, Yangzhou 225127, China
e-mail: zhangc@yzu.edu.cn

J.-Y. Xu, H.-L. Liao
ICB UMR 6303, CNRS, Univ. Bourgogne Franche-Comté, UTBM, Belfort 90010, France

M. Debliquy
Service de Science des Matériaux, Faculté Polytechnique, Université de Mons, Mons 7000, Belgium

Q.-Q. Liu
College of Agriculture, Yangzhou University, Yangzhou 225009, China

chromatography-mass spectrometry [7], have been extensively utilized for the detection of methanol. Except for superior precision and excellent stability, those methods generally suffer from several drawbacks (e.g., complicated procedures, high cost to maintain, large size and a lengthy detection period), significantly impeding them in the field of methanol sensing. Nowadays, gas sensors especially those based on metal oxide semiconductors because of portable, easy fabrication and real-time detection, have drawn great attention from the public.

Metal oxide semiconductors stand out among other gas sensors in the detection of methanol due to their outstanding characteristics including high physicochemical stability, cost-effective synthesis, and excellent sensing properties [8–10]. Gas sensor based on hollow α-Fe_2O_3 microspheres was constructed by Yang et al. [11] through a hydrothermal route. The sensor exhibited a superior sensitivity of 25.1 and rapid response/recovery times (8/9 s) towards 10×10^{-6} methanol at 280 °C. Song et al. [12] fabricated SnO_2 sensing materials with various morphologies through a simple hydrothermal approach. And the gas sensor based on SnO_2 nanoflowers showed a sensitivity of 1.6 towards 1×10^{-6} methanol vapors at 200 °C. Above all, those sensing results illustrated that these metal oxides were substantially utilized in the detection of methanol and received relatively outstanding sensing properties. However, the operating temperature, sensitivity and long-term stability should be improved. Presently, several effective methods including doping transition metals, surface modification, newly designed structure and morphology, and self-doping of oxygen vacancy have been proposed to optimize the features of metal oxide semiconductor gas sensors in methanol sensing [13, 14]. Nevertheless, in the process of elevating the sensing performance of metal oxides, they often require adding other oxides or precious metals to form compositions through two steps. And searching for sensing materials with newly designed structures and excellent physicochemical performance to significantly elevate the sensing properties towards methanol, ternary metal oxide semiconductor (II-IV-VI oxides) gas sensors have drawn increasing research interests because of their high structure controllability through a simple approach.

Among these ternary oxides, $ZnSnO_3$ with a face-centered perovskite structure is attracting more attention due to its outstanding physicochemical properties, high electrical conductivity and electron mobility, wide bandgap, and easy to synthesize various structures [15]. Besides, crystal and oxygen defects are more easily generated inside of the crystal structure and onto the surface of $ZnSnO_3$, and its unique position of Zn located at the gap of the regular octahedron consisted of six O atoms will be responsible for the enhanced sensing performance, especially for the analysis of reducing gases. Zhang et al. [16] prepared unique $ZnSnO_3/SnO_2$ microcubes through a facile liquid-phase reaction. The experiments delivered superior gas sensing characteristics including high response (18.3), rapid response/recovery times (5/6 s) and excellent reproducibility to 50×10^{-6} reducing gas (acetone) at 260 °C. Meanwhile, Cheng et al. [17] synthesized hollow $SnO_2/ZnSnO_3$ microspheres with various morphologies through chemical vapor deposition utilizing different amounts of sucrose as a solid template. At 290 °C, the sensitivity of gas sensor based on $SnO_2/ZnSnO_3$ with double-shelled microstructure was 30 towards 100×10^{-6} acetone. And this enhancement could be principally ascribed to hollow structures displaying a higher specific surface area (188.60 $m^2 \cdot g^{-1}$). Although gas sensors based on $ZnSnO_3$ possess the merits of high sensitivity, rapid response, and superior selectivity to VOCs, they still require being heated to a high working temperature (200–300 °C) to promote the adsorption/desorption of VOCs. Meanwhile, the synthesis procedures of $ZnSnO_3$ hierarchical composites are complex, and generally require two steps and/or a template. Consequently, it is necessary and urged to develop novel hierarchical $ZnSnO_3$ sensing materials for methanol sensing at low temperatures through a simple template-free step.

Herein, a simple template-free approach via regulating the molar ratio of Zn^{2+} and Sn^{4+} sources was proposed for interface engineering on self-assembled $ZnSnO_3$-based heterojunctions with different structures and morphologies (hollow spheres, hollow cubes, and octahedrons). It is ultimately expected that gas sensors based on $ZnSnO_3$ composites revealed much better sensing properties towards methanol than that of pure $ZnSnO_3$ at room temperature (RT), in which the hollow structure with high specific surface areas, the heterojunctions formed between $ZnSnO_3$ and ZnO or SnO_2 interfaces, the enhancement of dissociative and chemisorbed oxygen contents is primarily responsible for the outstanding RT sensing properties with a combination of low detection limit (0.49×10^{-6}), high sensitivity (10.16), and fast response/recovery times (14/75 s). Furthermore, this work concentrates on the sensing properties, also discussed the sensing mechanism towards methanol at RT. The outstanding sensing properties of $ZnO/ZnSnO_3$ were analyzed by density functional theory (DFT) calculations, and the experiments revealed that the special tuning effects of Zn ionic sites on methanol adsorption. Besides, the practical experiment revealed that $ZnO/ZnSnO_3$ gas sensor might be available for on-field dynamic methanol monitoring in the chemical reaction utilizing H_2 and CO_2 as raw materials. This research indicates that $ZnSnO_3$-based heterostructures have a tremendous potential application in methanol sensing, and provides a feasible route to regulate the structure and morphology of metal oxides.

2 Experimental

2.1 Synthesis of $ZnSnO_3$-based heterojunctions

$ZnSnO_3$-based heterojunctions with different structures and morphologies were prepared via a simple template-free method utilizing ethanol and deionized water as solvents. Typically, 3 mmol $Zn(NO_3)_2{\cdot}xH_2O$ and $SnCl_4{\cdot}5H_2O$ were dispersed into 90 ml alcohol-water solutions with a volume ratio of 1:2. After stirring for 10 min, 30 and 75 mmol NaOH were separately added again, forming a uniform solution. After alternately sonicating and stirring for 20 min, the solution was transformed into a round-bottom flask with a volume of 250 ml, and heating reflux at 80 °C for 3 h. After naturally cooled to RT, the as-synthesized powders were centrifuged with ethanol and deionized water, and finally dried at the temperature of 80 °C for 12 h. Then the as-obtained precipitates were annealed under an ambient atmosphere at 400 °C for 2 h with a heating rate of 3 °C·min^{-1}. Similarly, the molar ratio of $Zn(NO_3)_2{\cdot}xH_2O$ and $SnCl_4{\cdot}5H_2O$ was adjusted to $Zn(NO_3)_2{\cdot}xH_2O$ (6 mmol): $SnCl_4{\cdot}5H_2O$ (3 mmol) = 2:1 and $Zn(NO_3)_2{\cdot}xH_2O$ (3 mmol): $SnCl_4{\cdot}5H_2O$ (6 mmol) = 1:2. The as-prepared powders were marked as S1 (1:1), S2 (2:1) and S3 (1:2), respectively.

2.2 Materials characterization

Scanning electron microscope (SEM, S-4800) and transmission electron microscopy (TEM, Tecnai 12) combined with high-angle annular dark-field scanning transmission electron microscope (HAADFSTEM), selected area electron diffraction (SAED) and energy dispersive spectroscopy (EDS) were employed to characterize the structure and morphology of the three powders. And the phase compositions were examined by X-ray diffraction (XRD, Bruker D8 Advance). Additionally, ultraviolet–visible spectroscopy (UV-Vis) absorption spectra were investigated by a Cary 5000 spectrometer (670-IR + 610-IR), the existence of oxygen vacancy and the chemical states were inspected by photoluminescence (PL, He-Cd Lasers) and X-ray photoelectron spectroscopy (XPS, ESCALAB 250Xi). Moreover, their specific surface areas were investigated by Barret-Emmett-Teller (BET, Quadrasorb EVO) method based on nitrogen adsorption–desorption measurement.

2.3 Gas sensor fabrication and testing

The homogenous pastes obtained by mixing the powders with deionized water were dip-coated onto the surfaces of the sensors substrates, and then they were annealed at the temperature of 400 °C for 2 h with a heating rate of 2 °C·min^{-1} for aging before measurement to obtain more stable data. The gas-sensing testing of $ZnSnO_3$-based heterostructures was investigated utilizing a home-made gas equipment (HCRK-SD101). Prior to testing, all sensors are aged by flowing synthetic air until the electrical resistance is stable and marked as R_a. When the electrical resistance reaches a stable state again after the sensing materials contacted with methanol molecules. And the resistance is marked as R_g. And the response is calculated by the ratio of R_a and R_g.

3 Results and discussion

3.1 Structural and morphological characteristics

The structure and morphology of S1, S2 and S3 were demonstrated in Fig. 1. It can be observed from Fig. 1a that microspheres with a diameter of (1.5 ± 0.1) μm were fabricated via a template-free approach. And $ZnSnO_3$ microspheres revealed a porous and hollow structure with a shell thickness of around 240 nm (Fig. S1a), which was obtained by the self-assembly of $ZnSn(OH)_6$ particles [18]. While as Zn^{2+} sources increases, the as-obtained materials consist of uniform microcubes with a size of (1.3 ± 0.1) μm, and some particles are identified on the cube's surface, as illustrated in Fig. 1b. Besides, the sample also exhibits a hollow cube with a shell thickness of ~ 150 nm (Fig. S1b), which can enhance its specific surface area, contributing to promoting the transmission and diffusion of the target gas compared with S1. When the molar ratio of Zn^{2+} and Sn^{4+} sources was 1:2, S3 has an octahedral morphology with a smooth surface (Fig. 1c). Accordingly, $ZnSnO_3$-based sensing materials with diverse structures and morphologies were successfully synthesized by regulating the molar ratio of Zn^{2+} and Sn^{4+} sources based on a template-free approach. Moreover, Fig. 1d–f displays TEM morphologies of S1, S2 and S3, respectively. And the as-obtained structures are consistent with the images acquired from SEM analysis shown in Fig. 1a–c. Among them, bright contours at their centers and dark contours at their edges are depicted in Fig. 1d, e, further confirming that the hollow structure was formed in S1 and S2. While the hollow structure demonstrated in Fig. 1f is not identified. And to further investigate the crystallinity of S1 and S2, HRTEM combined with SAED analysis were employed. SAED image shown in Fig. 1g displays diverse diffraction circles, indicating that the crystal structure of S1 is low crystallinity. While it can be observed from Fig. 1h that the existence of some circular dot arrays in SAED pattern of S2 demonstrates the polycrystalline feature, indicating that the crystal feature has changed with an increase in the molar of Zn^{2+} sources. Besides, two distinct diffraction

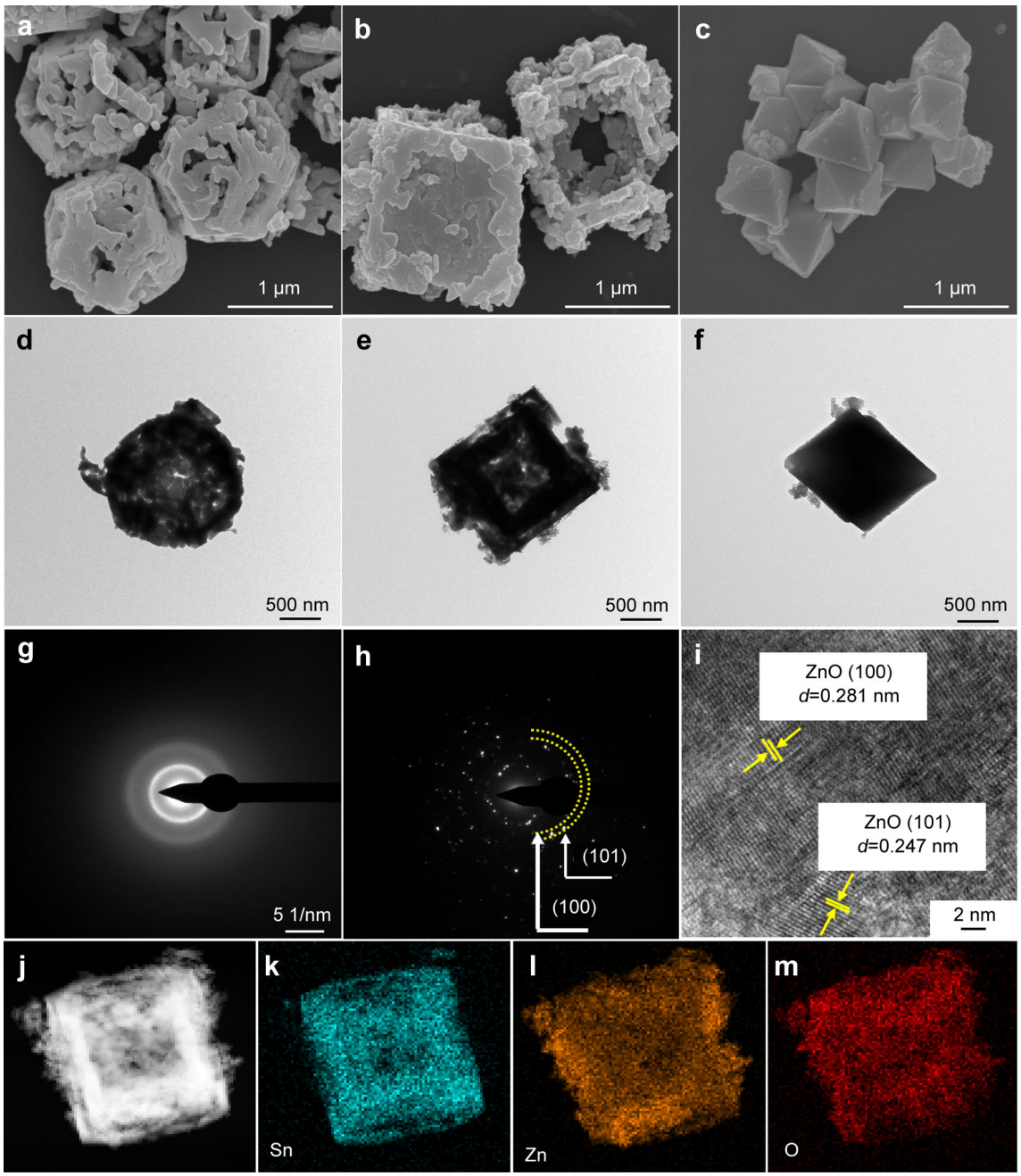

Fig. 1 **a**–**c** SEM images and **d**–**f** TEM images of S1, S2 and S3; SAED images of **g** S1 and **h** S2; **i** HRTEM image of S2; **j** HAADFSTEM image and **k**–**m** EDS elemental mappings of Zn, Sn, O in S1

rings assigned to the (101) and (100) crystal planes are detected. Meanwhile, the spacings of lattice fringe are 0.247 and 0.281 nm, corresponding to (101) and (100) planes of ZnO [19, 20], respectively, as illustrated in Fig. 1i. It can be deduced that the attached particles may be ZnO. Additionally, the chemical compositions of S1, S2 and S3 were investigated by EDS. The element mapping (Fig. 1k–m) reveals that Sn, Zn and O uniformly scatter throughout the samples. Especially for S2, the attached particles mainly consist of Zn and O, confirming that the heterojunctions might be formed between $ZnSnO_3$ and ZnO.

SEM and TEM observations reveal that the molar ratio of Zn^{2+} and Sn^{4+} sources has an important impact upon the formation of $ZnSnO_3$-based heterojunctions. And the synthesis procedures of S1, S2 and S3 are schematically illustrated in Fig. 2. In water-alcohol mixed solutions, NaOH was hydrolyzed into extensive OH^-, contributing to rapid hydrolysis of Zn^{2+} and Sn^{4+} at the temperature of 80 °C, and the assembly of $ZnSn(OH)_6$ particles (Fig. S2).

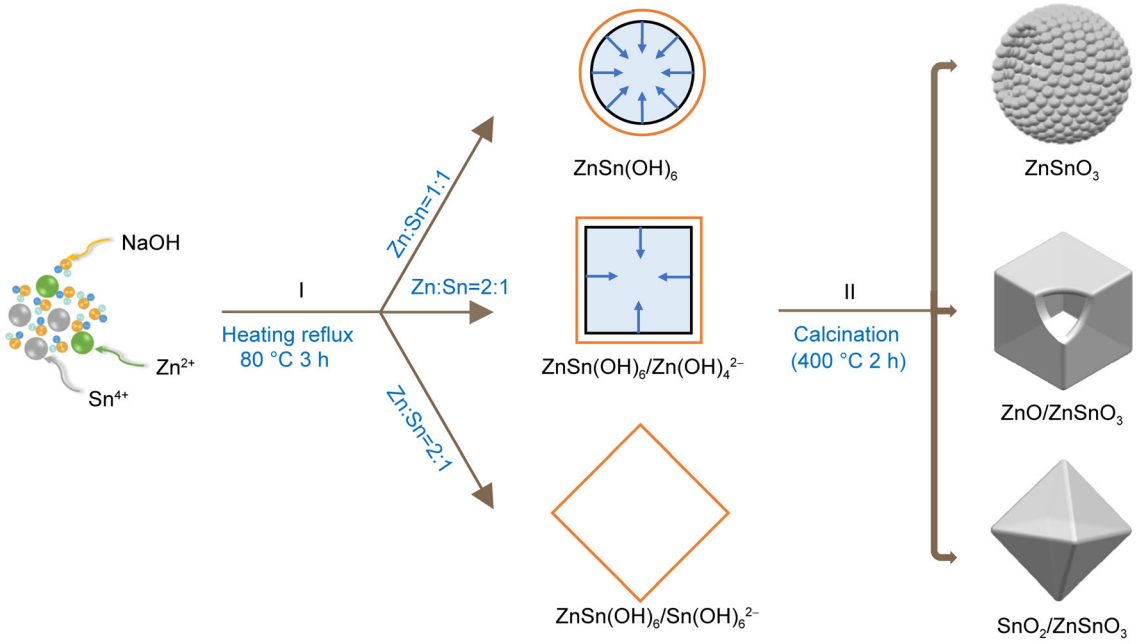

Fig. 2 Schematically illustration of formation procedure of $ZnSnO_3$ hierarchical microstructures (Step I: heating reflux with temperature of 80 °C and duration of 3 h; Step II: calcination with temperature of 400 °C and duration of 2 h

Specifically, the synthesis procedure of S2 chiefly involved the following steps. (I) $ZnSn(OH)_6$ precursors with cubic structures spontaneously formed via the complexation among Sn^{4+}, Zn^{2+} and OH^- under alkaline solutions (Eq. (1)) because of its inherent cubic microstructure. (II) Since there were a large number of OH^- attached to cube-shaped $ZnSn(OH)_6$ crystal's surface, excess Zn^{2+} sources could react with them to generate $Zn(OH)_4^{2-}$ anions (Eq. (2)), contributing to the formation of ZnO (Fig. 1e). (III) The ZnO/$ZnSnO_3$ composites were obtained by the calcination treatment (Eq. (3)). Meanwhile, the formation of hollow structure of S1 and S2 chiefly resulted from the alkaline etching via a dissolution process. Similarly, $ZnSn(OH)_6$ octahedron was formed and additional Sn^{4+} reacted with OH^- to generate $Sn(OH)_6^{2-}$ anions (Eq. (4)) in the preparation of S3. Subsequently, SnO_2/$ZnSnO_3$ heterojunctions were formed through annealing at 400 °C for 2 h under the ambient atmosphere (Eq. (5)). While the concentration of OH^- significantly decreased, and the etching could not continuously process. Hence the hollow structure in S3 was not observed.

$$Zn^{2+} + Sn^{4+} + 6OH^- \rightarrow ZnSn(OH)_6 \quad (1)$$

$$Zn^{2+} + 4OH^- \rightarrow Zn(OH)_4^{2-} \quad (2)$$

$$ZnSn(OH)_6 + Zn(OH)_4^{2-} \rightarrow ZnSnO_3 + ZnO + 4H_2O + 2OH^- \quad (3)$$

$$Sn^{4+} + 6OH^- \rightarrow Sn(OH)_6^{2-} \quad (4)$$

$$ZnSn(OH)_6 + Sn(OH)_6^{2-} \rightarrow ZnSnO_3 + SnO_2 + 5H_2O + 2OH^- \quad (5)$$

To give insight into the crystallographic structures of $ZnSnO_3$ hierarchical sensing materials synthesized via regulating the molar ratio of Zn^{2+} and Sn^{4+} sources, XRD analysis of S1, S2 and S3 given in Fig. 3a was performed. One broad peak can be identified in S1 and S3, demonstrating that the nature of the powders was amorphous and had a low crystallinity [21]. While in XRD spectrum of S2, the crystal structure dramatically changed and displayed a high crystalline, which was consistent with SAED pattern (Fig. 1h). Additionally, several distinct peaks with 2θ of 31.7°, 34.4°, 36.2°, 47.5°, 56.6° and 62.8° corresponding to (100), (002), (101), (102), (110) and (103) planes are well-matched with the hexagonal wurtzite structured ZnO (JCPDS No. 36–1451) [22], confirming that S2 sample is a mixture of $ZnSnO_3$ and ZnO phases. The reason for which is that $ZnSnO_3$ and Zn_2SnO_4 are generated at the temperature ranging from 300 to 500 °C and above 600 °C, respectively [23]. And excess Zn^{2+} sources were transformed into ZnO, being consistent with the result demonstrated in Fig. 1e. Meanwhile, the SnO_2 phase centered at around 60.7° was also detected in S3, proving that the powders generally consist of SnO_2 and $ZnSnO_3$. Accordingly, the heterojunctions were formed between $ZnSnO_3$ and ZnO or SnO_2 interfaces via regulating the molar ratio of Zn^{2+} and Sn^{4+} sources. To obtain more detailed information concerning their intrinsic characteristics, UV–Vis

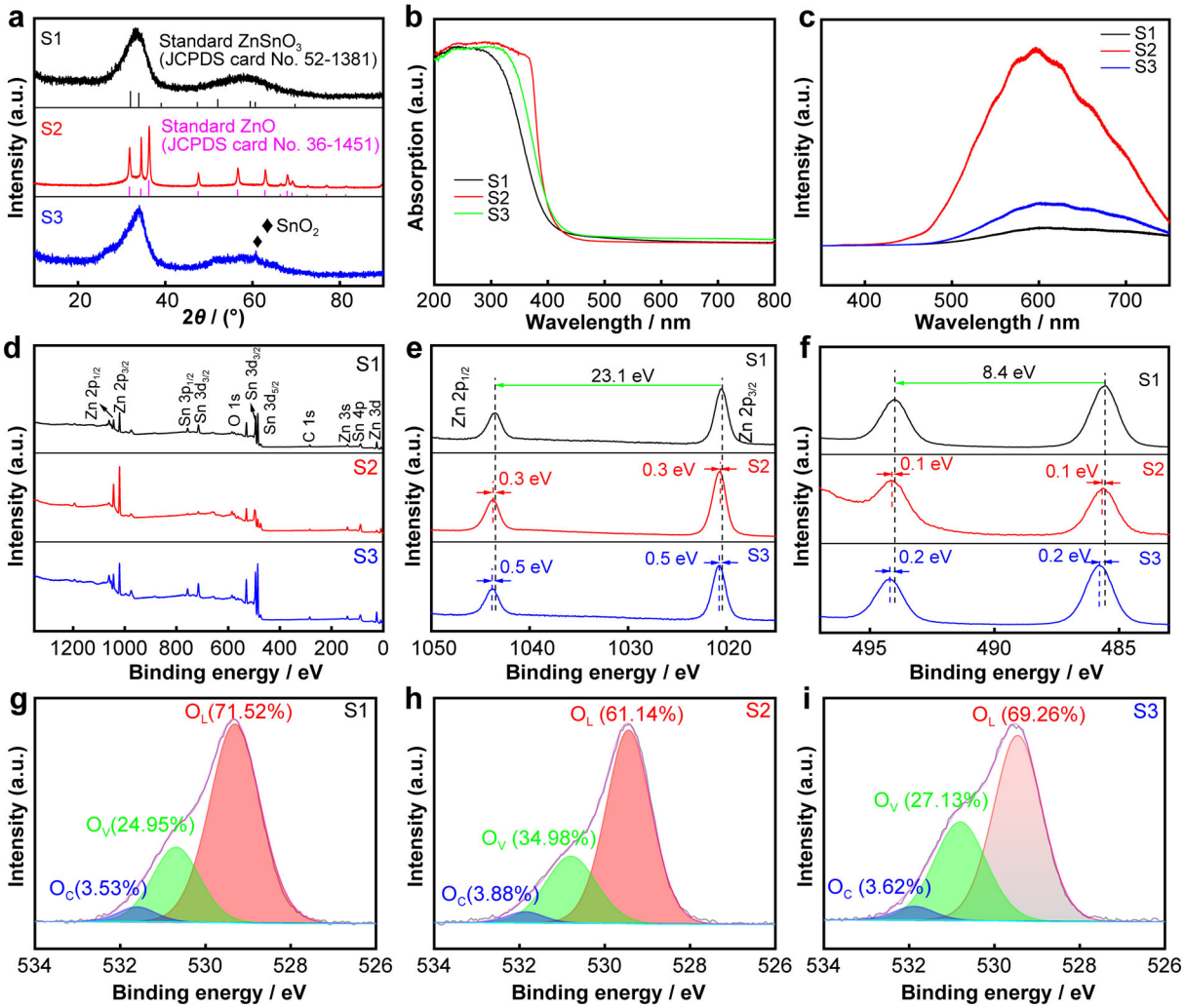

Fig. 3 **a** XRD patterns of three samples after calcination; **b** UV–Vis absorption spectra of three samples; **c** PL patterns of three samples; XPS analysis of three samples: **d** survey spectra, **e** Zn 2p spectra, **f** Sn 3d spectra, and **g–i** O 1s spectra

absorption of all samples was investigated, as shown in Fig. 3b. It is obvious that the absorption tails are found in both visible and near-infrared areas, which are closely related to the oxygen vacancy-induced polarons and/or free electrons [24]. Besides, the absorption edge of S2 and S3 exhibits an obvious shift towards a large wavelength, suggesting the presence of various concentrations of oxygen vacancy in the sample. To confirm it, PL analysis was employed to inspect the existence of oxygen vacancy in the powders. As depicted in Fig. 3c, there is a defect luminescence peak with a wavelength ranging from 450 to 750 nm, which is mainly connected to the electronic transition between oxygen vacancy and conduction band of $ZnSnO_3$ [25]. Moreover, the intensity of the defect luminescence peak of S2 and S3 become stronger than that of S1, demonstrating a larger proportion of oxygen vacancy existed in the sample. Meanwhile, the chemical states and oxygen species of all samples were characterized via XPS. The survey spectra given in Fig. 3d display the presence of Zn, Sn and O, well-matched with the EDS provided in Fig. 1k–m. At the same time, it can be observed from Fig. 3e that there are two peaks located at 1021.7 and 1044.8 eV, which are respectively assigned to Zn $2p_{3/2}$ and Zn $2p_{1/2}$ for S1. And the spin–orbit splitting of the two peaks is 23.1 eV, demonstrating that the valence state of Zn atom is + 2 [26]. And the binding energies of S2 and S3 are 0.3 and 0.5 eV higher than that of S1, which indicates that the lower electron density is due to the interaction between $ZnSnO_3$ and ZnO or SnO_2 [19]. The spectrum of Sn 3d is consistent with Zn 2p, as demonstrated in Fig. 3f. The spin–orbit between Sn $3d_{5/2}$ and Sn $3d_{3/2}$ shows a split value of 8.4 eV, suggesting an oxidation state + 4 of Sn [27]. Besides, O 1s spectra depicted in Fig. 3g–i can be deconvolved into three Gaussian-Lorenz peaks located at 529.3, 530.6 and 531.5 eV, corresponding to different types of oxygen

species including O_L (lattice oxygen), O_V (dissociative oxygen) and O_C (chemisorbed oxygen) [17]. Among them, O_V caused by oxygen antisite defects, oxygen vacancies and oxygen gaps can directly react with methanol molecules. Besides the integrated areas of the three peaks were calculated (Table S1). The proportions of various oxygen species of the three samples have been provided in Fig. 3g–i. Among them, the proportion of O_V in S2 is 34.99%, which is higher than that of S1 (24.95%), which may be associated with the formation of heterojunctions by regulating the molar ratio of Zn^{2+} and Sn^{4+} sources. This improvement can offer more active adsorptive sites for methanol sensing in the redox reaction, promoting the carrier transfer and enhancing the RT sensing properties towards methanol.

3.2 Gas sensing performance

The gas sensing properties towards ppm-level methanol were comprehensively investigated by a gas sensing setup operating under the ambient conditions including the temperature of (25 ± 1) °C and the relative humidity (RH) of 30% ± 10%, as schematically demonstrated in Fig. 4a and Fig. S3. The changes in the resistance of all sensors towards various concentrations (1×10^{-6}-5×10^{-6}) of methanol are shown in Fig. 4b. As a characteristic n-type metal oxide, the electrical resistance sharply increased when $ZnSnO_3$-based sensors were exposed to purified air ($79\%N_2 + 21\%O_2$), and eventually exhibited a relatively stable state (R_a) ranging from 0.1 to 10.0 GΩ. When methanol molecules were exposed, the sensor resistance decreased and ultimately reached saturation (R_g). Once purified air was introduced, the electrical resistance of all sensors could return to the initial values (R_a). Additionally, compared with S1, the electrical resistance (R_a) of S2 and S3 decreased, which was highly dependent on the gas sensing materials [28]. Herein, the molar ratio of Zn^{2+} to Sn^{4+} sources in S1, S2 and S3 is 1:1, 2:1 and 1:2. And based on the analysis of the XRD pattern, S2 and S3 are composed of ZnO and $ZnSnO_3$, SnO_2 and $ZnSnO_3$ respectively, while S1 exhibits pristine $ZnSnO_3$ phases. Accordingly, the order of R_a is S1 > S3 > S2 due to the formation of heterojunctions and the elevated percentage of O_V and O_C [29]. According to the variations of resistance shown in Fig. 4b, the linear correlation between sensor sensitivity and concentration (1×10^{-6}–5×10^{-6}) of methanol is displayed in Fig. 4c. Apparently, all sensors display a positive linear relationship, and S3 displays the highest sensitivity of 10.16 towards 5×10^{-6} methanol with a theoretical limit of detection (0.49×10^{-6}) obtained via the equations provided in the reference [30]. The enhancement in sensitivity is nearly consistent with the order of the concentration of O_V measured by XPS, which is generally because of the hollow structure, the existence of oxygen vacancy effectively improving the content of chemisorbed oxygen species and the construction of heterojunctions at the interfaces between $ZnSnO_3$ and ZnO or SnO_2. Furthermore, the specific surface area and pore size distribution (Fig. S4, Table S2) display that S2 exhibits a larger specific surface area (21.320 $m^2 \cdot g^{-1}$ for S1, 42.277 $m^2 \cdot g^{-1}$ for S2 and 25.402 $m^2 \cdot g^{-1}$ for S3) and a larger pore size distribution (2.972 nm for S1, 3.714 nm for S2 and 3.322 nm for S3), dramatically improving the permeability of methanol gas molecules and promoting their rapid diffusion [31, 32]. As evident in Fig. 4d, the dynamic response-recovery curves to 5×10^{-6} methanol were investigated to evaluate the sensing properties of S1, S2 and S3. It can be calculated that the response time (τ_{res}) and recovery time (τ_{rec}) are 21/82 s (S1), 14/75 s (S2) and 17/78 s (S3). The short τ_{res} can be due to its unique hollow structure, which is advantageous to the diffusion of methanol among the sensing materials. While τ_{rec} is still long (> 1 min), principally because the sensor operated at RT does not provide sufficient activation energy for methanol desorption [33]. In addition, the shell thickness of S2 is smaller than that of S1 (Fig. S1), further accelerating methanol desorption. Given in the factor that the sensor exclusively responding to the target gas is a key index for its practical application, the selectivity of the three sensors towards a variety of gases (NO_2, SO_2, NH_3, CO_2, ethanol, and isopropanol) with the concentration of 5×10^{-6} was investigated, as reflected in Fig. 4e. Obviously, all sensors show the highest sensitivity towards methanol under various interfering gases. Among them, ZnO/$ZnSnO_3$ sensor has the highest response and excellent selectivity to methanol over ethanol. This is mainly attributed to the electron energy of chemisorbed oxygen being similar to the lowest unoccupied molecules orbit energy of methanol gas molecules and improving the redox reaction between methanol and oxygen species [34]. Consequently, the as-developed sensor exhibits outstanding selectivity to methanol at RT. Moreover, to verify the repeatability of the sensor, the sensitivity of S2 towards 5×10^{-6} methanol within five cycles manifested in Fig. 4f was analyzed, and there are no obvious changes in R_a and sensitivity with the deviation of 5.2% and 9.7%, indicating the outstanding repeatability in methanol sensing. Additionally, long-term stability is also an essential factor in assessing the service life of gas sensors. As illustrated in Fig. 4g, both response and R_a of S2 still remain stable and the sensitivity towards 5×10^{-6} methanol maintains above 90% within 30 days, demonstrating excellent long-term stability. Moreover, it is reported that RH has a substantial influence upon the sensing performance of gas sensors. And the influence of RH on sensor response and R_a of S2 was also investigated. The sensor response towards 5×10^{-6} methanol under

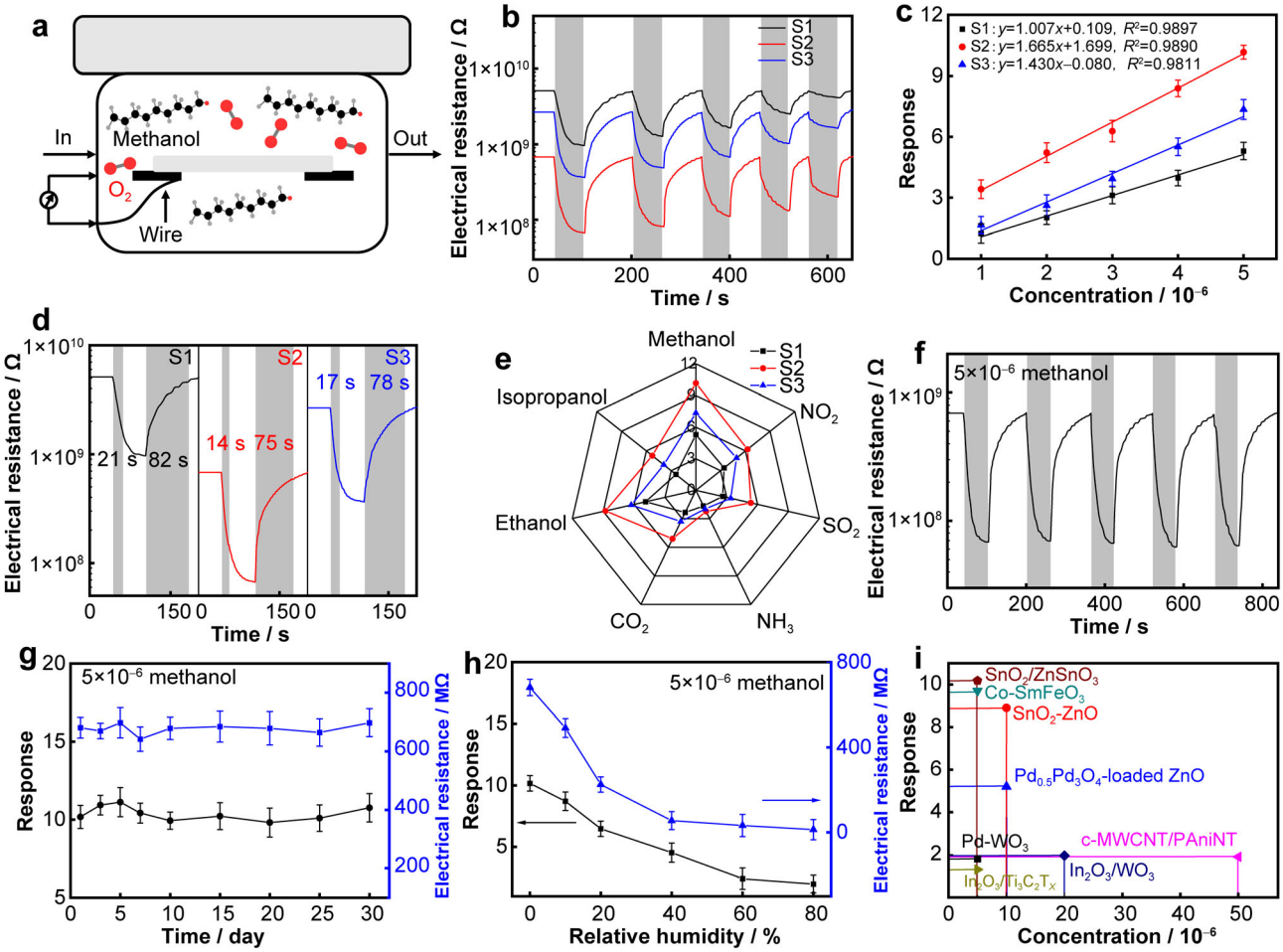

Fig. 4 **a** Schematic illustration of sensing measurement setup; **b** changes in electrical resistance towards different concentrations (1×10^{-6}–5×10^{-6}) of methanol; **c** linear relationship between sensor responses and concentrations; **d** response time (τ_{res}) and recovery time (τ_{rec}) of S1, S2 and S3 to 5×10^{-6} methanol; **e** sensor responses of S1, S2 and S3 to different target gases of 5×10^{-6}; **f** reproducibility of S2 to 5×10^{-6} methanol; **g** long-term stability including response and resistance of S2 to 5×10^{-6} methanol; **h** sensor responses and its corresponding resistance of S2 to 5×10^{-6} methanol under various RH (0, 10%, 20%, 40%, 60% and 80%); **i** gas-sensing performance in comparison with other state-of-the-art methanol sensors

various RH atmospheres (10, 20%, 40%, 60% and 80%) at RT was analyzed (Fig. S5). Figure 4h concludes that R_a decreases with RH increasing. Since water molecules occupy the adsorption sites originally belonging to oxygen species, and hinder the target gas adsorption, both sensitivity and R_a of S2 in the detection of methanol dramatically decrease. To reduce the effect of humidity, depositing a functional sensing layer onto the surface of $ZnSnO_3$-based composites, chemically modulating the sensing material and constructing appropriate humidity compensation models can be extensively utilized in future research [35, 36]. Besides, the gas-sensing properties compared with other methanol sensors are comparatively shown in Fig. 4i, and detailed information containing its morphology, sensitivity, working temperature and RH in the detection of methanol is illustrated (Table S3). And those experiments show that S2 with hollow cubic structures and extensive oxygen vacancies reveals a superior response even at a relatively low concentration of methanol. Consequently, it is an advanced gas sensor based on hollow ZnO/$ZnSnO_3$ microcubes for methanol sensing at RT.

To understand the superior sensing performance, DFT calculations were employed to calculate the adsorption energy and the charge transfer when the methanol molecules adsorbed onto the ZnO/$ZnSnO_3$ surface. To evaluate the adsorption energy of methanol on ZnO/$ZnSnO_3$, the density of states (DOS) as a function of energy (eV) of the individual elements were calculated based on methanol gas molecules binding at their neighboring sites. As demonstrated in Fig. 5a, it is obvious that the Zn ions are responsible for facilitating the DOS around the Fermi energy level and assisting in the conduction [37]. Accordingly, Zn 2p peaks lying near Fermi energy level have a substantial effect on the electron donation and

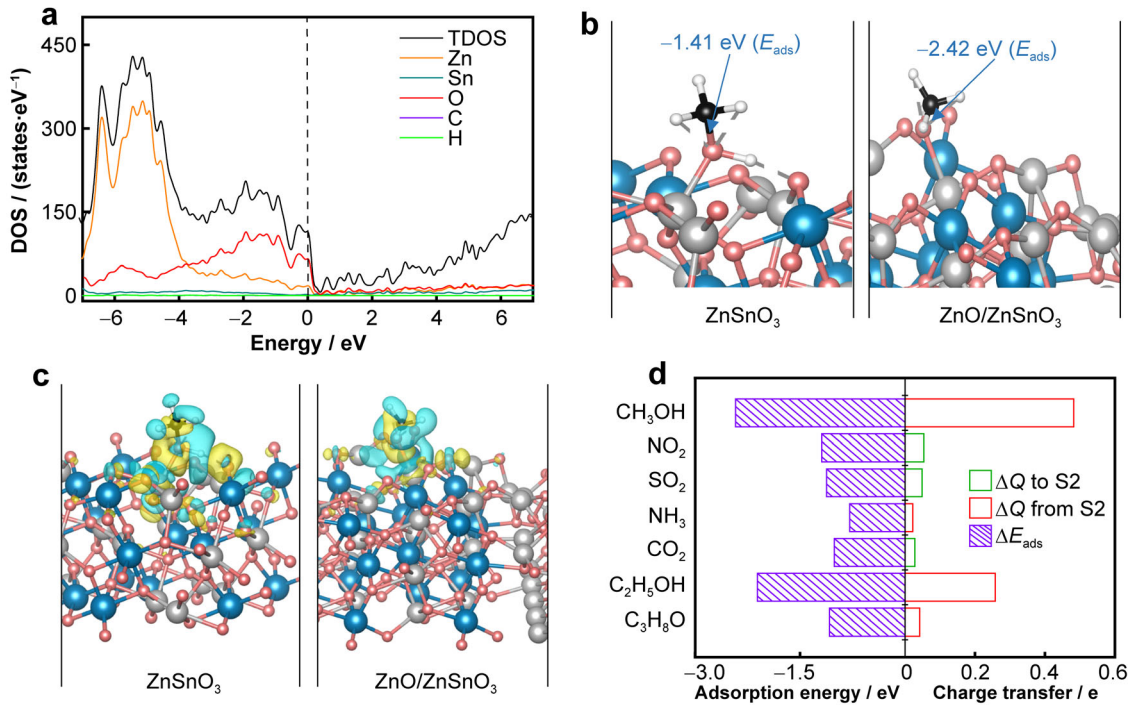

Fig. 5 **a** Total density of states plots for methanol adsorption; **b** corresponding methanol adsorption geometries, where Sn, Zn, O, C, and H atoms are shown in blue, red, gray, black, and white balls, respectively; **c** calculated differential valence-electron charge densities of methanol adsorption for $ZnSnO_3$ and $ZnO/ZnSnO_3$ ($\Delta\rho = \rho_{surface+methanol} - \rho_{surface} - \rho_{methanol}$) *(charge depletion and accumulation regions are illustrated by blue and yellow, respectively).* ***d*** *Calculated adsorption energies (left side) and charge transfer (right side) for various interfering gases on the S2 surface (charge transferred from and to the surface is plotted in red and green, respectively)*

strongly binding with methanol molecules. Meanwhile, the interaction between the surface of $ZnSnO_3$ or $ZnO/ZnSnO_3$ pre-adsorbed with O_2^- and methanol molecules was investigated to explain the sensing mechanism. Figure 5b shows the initial adsorption structures of $ZnSnO_3$ and $ZnO/ZnSnO_3$. And the calculated adsorption energy (E_{ads}) is negative, suggesting that the adsorption interaction of methanol molecules on the $ZnSnO_3$ and $ZnO/ZnSnO_3$ surface is spontaneous [38, 39], and the E_{ads} of $ZnO/ZnSnO_3$ heterojunctions is much lower than that of $ZnSnO_3$ and ZnO (Fig. S6), suggesting that the redox reaction between $ZnO/ZnSnO_3$ surface and methanol is more likely to proceed.

The above findings reveal that Zn ions on the $ZnO/ZnSnO_3$ surface are the active site for methanol gas molecules adsorption. Hence, $ZnO/ZnSnO_3$ surface with O atom adsorbed at the Zn position is chosen as the pre-adsorbed surface. Then methanol replaces O_2^- and directly adsorb on Zn sites on the surface via ionic bonds. Meanwhile, this adsorption interaction is accompanied by charge transfers, dramatically changing the resistance of $ZnO/ZnSnO_3$, resulting in the improved sensitivity towards methanol at RT [32, 40]. Additionally, the differential electron density of the adsorption of methanol molecules on the Zn positions was further analyzed to investigate the process of charge transfer at those positions. The results shown in Fig. 5c depict that charge transfer generally occurs inside the hydroxyl groups of methanol gas molecules, and between methanol and O_2^-. When methanol is adsorbed on the surface of $ZnO/ZnSnO_3$, the charge transfer proceeds between O–H bonds of the hydroxyl group, improving the electron transfer from $ZnO/ZnSnO_3$ heterojunctions to the adsorbed methanol gas molecules at the Zn ionic sites. Furthermore, DFT calculations of the adsorption energy and the charge transfer for other gases (NO_2, SO_2, NH_3, CO_2, ethanol, and isopropanol) selected for verifying the selectivity of the sensor. In Fig. 5d, the values of E_{ads} and charge transfer display a similar trend to the sensor sensitivity displayed in Fig. 4e, indicating that the excellent selectivity for methanol adsorption is chiefly due to the prominent charge transfer from the surface of $ZnO/ZnSnO_3$ to methanol (the structure of the adsorption geometries is revealed in Fig. S7) [41].

3.3 Methanol gas-sensing mechanism

As schematically depicted in Fig. 6, the sensing mechanism of S1, S2 and S3 towards methanol at RT is

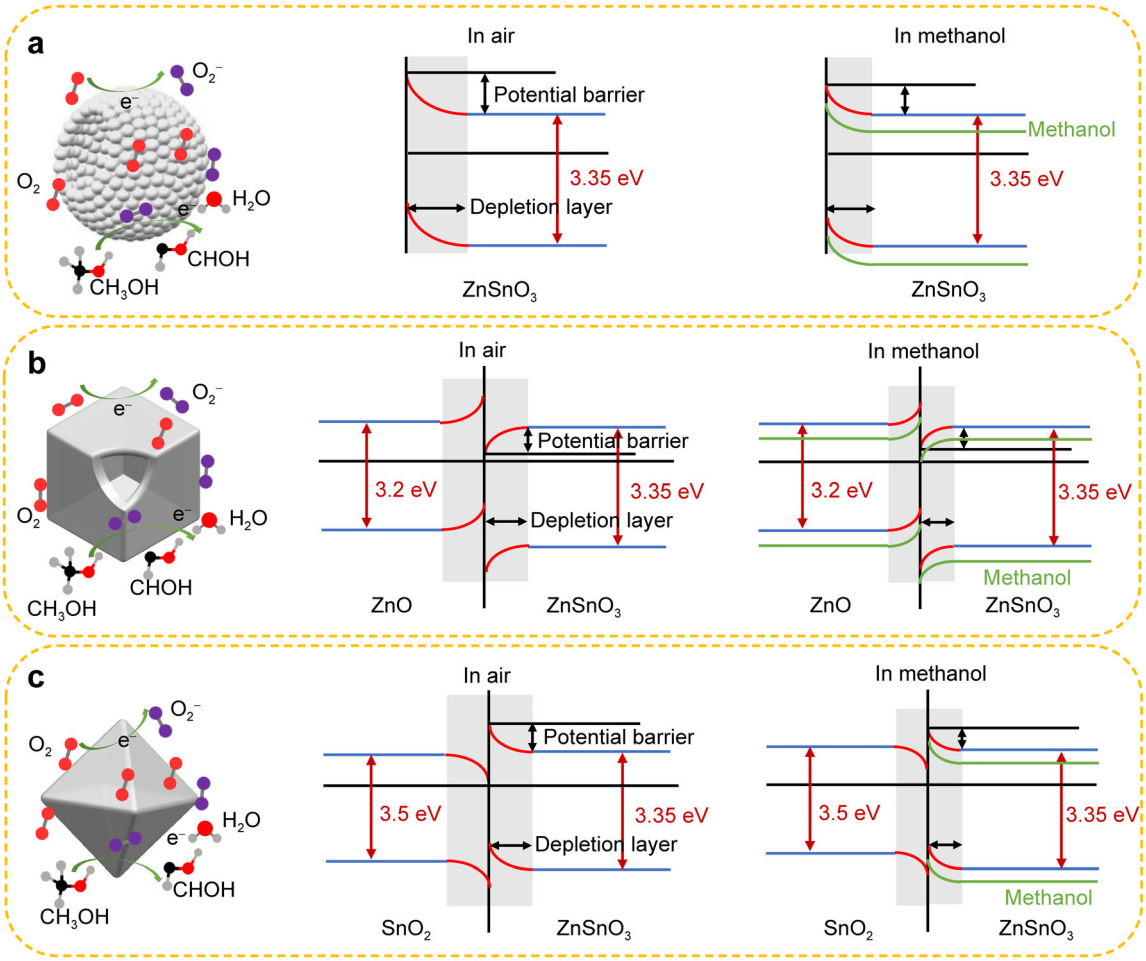

Fig. 6 Schematic illustrations of RT sensing mechanism of gas sensors based on: **a** $ZnSnO_3$ microspheres; **b** $ZnO/ZnSnO_3$ microcubes; **c** $SnO_2/ZnSnO_3$ octahedrons exposed to purified air ($71\%N_2 + 29\%O_2$) and methanol molecules

proposed. As typical n-type metal oxides, the adsorption mechanism of the three samples can be understood through the space-charge layer modes [42, 43]. Specifically, the $ZnSnO_3$-based sensing material's surfaces were adsorbed by oxygen molecules when the sensor contacted with the purified air. Subsequently, oxygen captured free electrons from the conduction band of the sensing materials at RT to generate chemically adsorbed oxygen species (O_2^-) [25], forming the potential barrier and the electron depletion region (Fig. 6a-c), resulting in decreasing the electron concentration of the sensing layers [44], and ultimately increasing the sensor resistance. Furthermore, heterojunctions with unique interface electronic effects were formed at the interfaces between n-type $ZnSnO_3$ and n-type ZnO or SnO_2 due to different gap energies and work functions, as shown in Fig. 6b and c. Among them, since the conduction band edge of $ZnSnO_3$ (-4.2 eV) is located at a lower potential than that of ZnO (-4.1 eV), the electrons transferred from the conduction band of ZnO to that of $ZnSnO_3$ until their Fermi level reached equilibrium [45–47]. In addition, an additional electron depletion and accumulation region were separately generated on the surface of ZnO and $ZnSnO_3$, reducing the amount of grain boundary barriers and contributing to a decrease in the resistance (R_a), which were conducive to enhancing the sensing performance of $ZnO/ZnSnO_3$ composites through promoting the redox reaction between methanol and sensing materials. Whereas reversal behaviors were obtained when heterojunctions were generated between $ZnSnO_3$ and SnO_2 interfaces owing to a higher Fermi level of $ZnSnO_3$. When the reducing gas (methanol) was exposed, CH_3OH (g) was first converted into adsorbed CH_3OH molecules (Eq. (6)). Then the redox reaction between CH_3OH (ad) and O_2^- was carried out, and producing CHOH (ad) (the loss of H), H_2O (g) and free electrons (Eq. (7)). In the redox reaction, the trapped electrons returned to the conduction band of $ZnSnO_3$-based composites, reducing the height of potential barrier and the thickness of depletion region (Fig. 6a–c) [48, 49], displaying the decrease of resistance.

$$CH_3OH(g) \rightarrow CH_3OH(ad) \quad (6)$$

$$2CH_3OH(ad) + O_2^-(ad) \rightarrow 2CHOH(ad) + 2H_2O(g) + e^- \quad (7)$$

The outstanding sensing properties of Z nO/$ZnSnO_3$ for the analysis of methanol at RT are primarily related to hollow cubic structure with high specific surface areas (42.277 $m^2 \cdot g^{-1}$), the formation of heterojunctions and the increased proportion of O_C and O_V. The hollow structure provides an effective route for the transmission and diffusion of methanol. And more active sites are available for methanol adsorption. Then the utilization rate of the sensing materials improves, thus elevating sensing properties. Moreover, the n–n heterojunctions are generated at the interfaces between $ZnSnO_3$ and ZnO. As illustrated in Fig. 6b, due to the construction of the depletion region, the potential barrier of $ZnSnO_3$-based sensing materials increases after the introduction of purified air, and the electron transfer becomes harder. While the methanol molecules can react with O_2^- after the introduction of the target gas. Meanwhile, electrons are released into the sensing materials and an additional electronic depletion region is generated between $ZnSnO_3$ and ZnO interfaces, resulting in increasing the electron concentration, which is beneficial to decrease the height of the potential barrier and the thickness of depletion region, ultimately accelerating the adsorption and/or desorption of methanol. Additionally, the increased proportions of O_C and O_V can return the negative charges to $ZnSnO_3$-based sensing material's conduction band, and the low connection area in heterojunctions reduces the height of potential barrier, significantly improving its electronic conductivity.

3.4 Practical experiments

Currently, hydrogen (H_2) is utilized as a raw material to synthesize methanol from carbon dioxide (CO_2), being one of common industrial waste gases. Under the condition of 298 K (~ 25 °C), the synthesis of methanol according to the chemical reaction between H_2 and CO_2 is shown in Eq. (8). To assess the practicability of the fabricated ZnO/$ZnSnO_3$ sensors in the detection of methanol, the variations of resistance of ZnO/$ZnSnO_3$ sensor contacted with H_2, CO_2 and their mixtures were monitored (Fig. 7a). It can be observed from Fig. 7b that the sensitivity towards H_2 and CO_2 mixtures is 17.72, which is around 5.5 and 8.9 times higher than that of H_2 (3.25) and CO_2 (1.99),

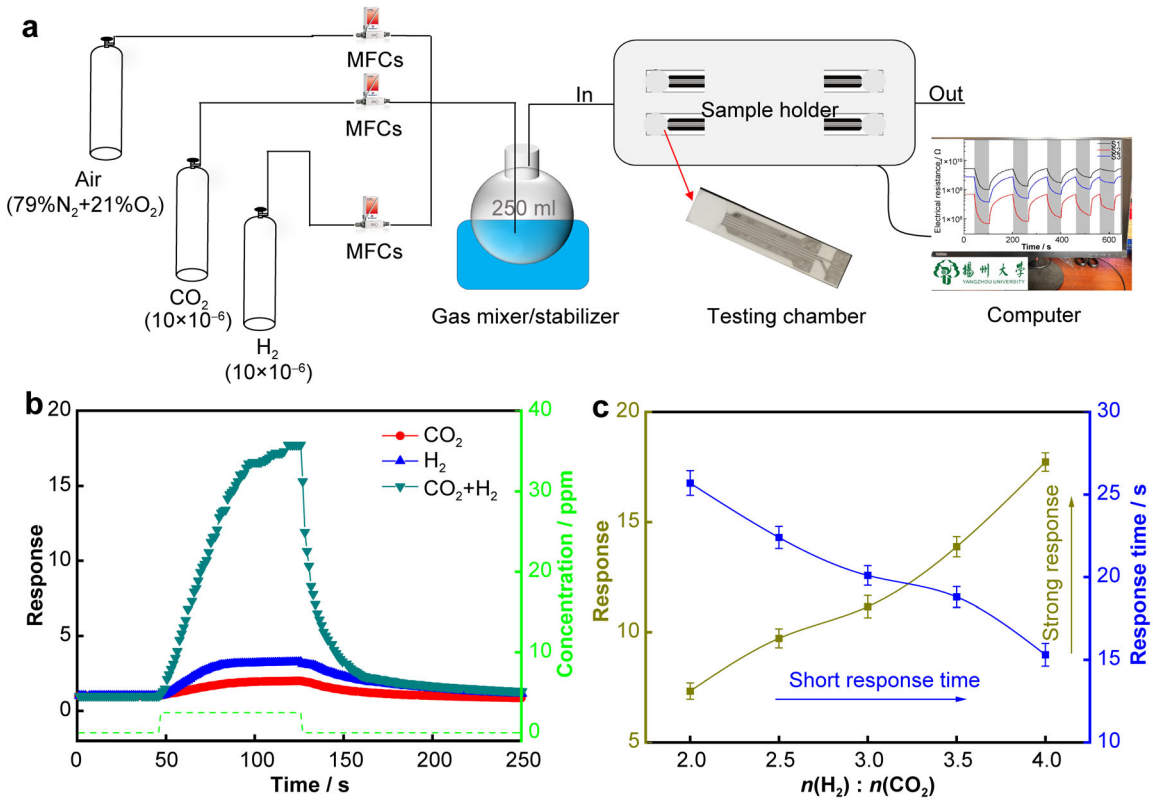

Fig. 7 **a** Schematic diagram of sensor testing system utilized in practicability testing based on hollow ZnO/$ZnSnO_3$ microcubes gas sensor; **b** responses measured under exposure to CO_2, H_2 and their mixtures; **c** sensors response and response times towards mixtures with increase of H_2 and CO_2 ratio

demonstrating that the chemical reaction between H_2 and CO_2 occurs, and methanol is simultaneously generated. Besides, to investigate the effect of the ratio of H_2 and CO_2, Fig. 7c reveals the response values and times towards the mixtures with the increase of H_2 and CO_2 ratio. Based on the variations of resistance (Fig. S8), the corresponding sensitivity and response times were calculated. It obvious that a high sensitivity is accompanied by a short response speed, indicating the concentration of methanol significantly increasing. Consequently, we conclude that increasing the content of H_2 can effectively promote the conversion of CO_2 and the yield of methanol. Those experimental results exhibit that ZnO/$ZnSnO_3$ gas sensor is capable of identifying methanol in the reaction.

$$\begin{aligned} CO_2(g) + 3H_2(g) &\rightarrow CH_3OH(g) + H_2O(g)\Delta H \\ &= -48.97\ \text{kJ} \cdot \text{mol}^{-1},\ \Delta S \\ &= -177.16\ \text{J} \cdot \text{mol}^{-1} \cdot \text{K}^{-1} \end{aligned} \quad (8)$$

4 Conclusion

In this work, a facile template-free approach through regulating the molar ratio of Zn^{2+} and Sn^{4+} sources is proposed for interface engineering on self-assembled $ZnSnO_3$-based heterojunctions, which are available for the methanol sensing at RT. The structural characterization indicates that hollow $ZnSnO_3$ microspheres, hollow ZnO/$ZnSnO_3$ microcubes and SnO_2/$ZnSnO_3$ octahedrons were successfully synthesized. Besides, the sensing characteristics of the three sensors were comprehensively investigated at RT. The sensing results reveal that hollow cubic ZnO/$ZnSnO_3$ sensor displays outstanding RT sensing properties towards ppm-level methanol. The elevated sensing properties are closely associated with the following aspects. The unique hollow cubic structures with large specific surface areas are advantageous for the transmission and diffusion of methanol. The construction of n–n heterojunctions formed at $ZnSnO_3$ and ZnO interfaces increases the thickness of depletion region and the height of potential barrier, elevating the concentration of electron. The enhanced relative proportion of O_V and O_C provides more adsorptive sites for methanol sensing. The DFT calculations indicates that it is Zn ions on ZnO/$ZnSnO_3$ surface that are the active adsorption sites, which is mainly responsible for the outstanding sensing properties for methanol adsorption because it offers a larger charge transfer and comparable adsorption energy. Furthermore, the practical experiments also demonstrates that ZnO/$ZnSnO_3$ can identify methanol in the chemical reaction utilizing H_2 and CO_2 as raw materials. And ZnO/$ZnSnO_3$ exhibits tremendous potential for room-temperature methanol sensing, and this study can offer a promising route for regulating the structure and morphology of metal oxide semiconductors.

Acknowledgements This study was financially supported by the Outstanding Youth of Jiangsu Province of China (No. BK20211548), the China Scholarship Council (No. 202108320264) and the Excellent Doctoral Dissertation Fund of Yangzhou University (2022).

Declarations

Conflict of interests The authors declare that they have no conflict of interest.

References

[1] Dong C, Yang JJ, Xie LH, Cui GL, Fang WH, Li JR. Catalytic ozone decomposition and adsorptive VOCs removal in bimetallic metal-organic frameworks. Nat Commun. 2022;13(1):4991. https://doi.org/10.1038/s41467-022-32678-2.

[2] Acharyya S, Nag S, Kimbahune S, Ghose A, Pal A, Guha PK. Selective discrimination of VOCs applying gas sensing kinetic analysis over a metal oxide-based chemiresistive gas sensor. ACS Sens. 2021;6(6):2218. https://doi.org/10.1021/acssensors.1c00115.

[3] Wang MC, Zhang Z, Zhong HX, Huang X, Li W, Hambsch M, Zhang PP, Wang ZY, St Petkov P, Heine T, Mannsfeld SCB, Feng XL, Dong RH. Surface-modified phthalocyanine-based two-dimensional conjugated metal-organic framework films for polarity-selective chemiresistive sensing. Angew Chem Int Ed. 2021;60(34):18666. https://doi.org/10.1002/anie.202104461.

[4] Zhang PP, Zhao F, Shi W, Lu HY, Zhou XY, Guo YH, Yu GH. Super water-extracting gels for solar-powered volatile organic compounds management in the hydrological cycle. Adv Mater. 2022;34(12):2110548. https://doi.org/10.1002/adma.202110548.

[5] Li MQ, Yang RW, Zhang H, Wang SL, Chen D, Lin SY. Development of a flavor fingerprint by HS-GC-IMS with PCA for volatile compounds of Tricholoma matsutake Singer. Food Chem. 2019;290:32. https://doi.org/10.1016/j.foodchem.2019.03.124.

[6] Wu XY, Li Y, Zhang GK, Chen H, Li J, Wang K, Pan Y, Zhao Y, Sun YF. Photocatalytic CO_2 conversion of $M_{0.33}WO_3$ directly from the air with high selectivity: insight into full spectrum-induced reaction mechanism. J Am Chem Soc. 2019;141(13):5267. https://doi.org/10.1021/jacs.8b12928.

[7] Lu WY, Su XY, Klein MS, Lewis IA, Fiehn O, Rabinowitz JD. Metabolite measurement: Pitfalls to avoid and practices to follow. Annu Rev Biochem. 2017;86:277. https://doi.org/10.1146/annurev-biochem-061516-044952.

[8] Xu JY, Liu KW, Zhang C. Electronic nose for volatile organic compounds analysis in rice aging. Trends Food Sci Technol. 2021;109:83. https://doi.org/10.1016/j.tifs.2021.01.027.

[9] Li DY, Lu YL, Zhang C. Research progress of functional coatings prepared by suspension plasma spraying. Chin J Rare Met. 2022;46(11):1506. https://doi.org/10.13373/j.cnki.cjrm.XY21050002.

[10] Zhang C, Xu JY, Li HP, Liao HL. Role of ruthenium incorporation on room-temperature nonanal sensing properties of Ru-loaded urchin-like $W_{18}O_{49}$ hierarchical nanostructure. Sens Actuator B Chem. 2022;353:131096. https://doi.org/10.1016/j.snb.2021.131096.

[11] Yang HM, Ma SY, Yang GJ, Jin WX, Wang TT, Jiang XH, Li WQ. High sensitive and low concentration detection of methanol by a gas sensor based on one-step synthesis α-Fe_2O_3 hollow spheres. Mater Lett. 2016;169:73. https://doi.org/10.1016/j.matlet.2016.01.098.

[12] Song LM, Zhao B, Ju XN, Liu L, Gong YM, Chen WB, Lu BL. Comparative study of methanol gas sensing performance for

SnO_2 nanostructures by changing their morphology. Mater Sci Semicond Process. 2020;111:104986. https://doi.org/10.1016/j.mssp.2020.104986.
[13] Wang YC, Wu JM. Effect of controlled oxygen vacancy on H_2-production through the piezocatalysis and piezophototronics of ferroelectric R3C $ZnSnO_3$ nanowires. Adv Funct Mater. 2019;30(5):1907619. https://doi.org/10.1002/adfm.201907619.
[14] Zhang H, Zhang DZ, Wang DY, Xu ZY, Yan Y, Zhang B. Flexible single-electrode triboelectric nanogenerator with MWCNT/PDMS composite film for environmental energy harvesting and human motion monitoring. Rare Met. 2022;41(9):3117. https://doi.org/10.1007/s12598-022-02031-z.
[15] Sá BS, Zito CA, Perfecto TM, Volanti DP. Porous $ZnSnO_3$ nanocubes as a triethylamine sensor. Sens Actuator B Chem. 2021;338:129869. https://doi.org/10.1016/j.snb.2021.129869.
[16] Zhang JT, Jia XH, Lian DD, Yang J, Wang SZ, Li Y, Song HJ. Enhanced selective acetone gas sensing performance by fabricating $ZnSnO_3/SnO_2$ concave microcube. Appl Surf Sci. 2021;542:148555. https://doi.org/10.1016/j.apsusc.2020.148555.
[17] Cheng PF, Lv L, Wang YL, Zhang Y, Zhang YQ, Lei ZH, Xu LP. $SnO_2/ZnSnO_3$ double-shelled hollow microspheres based high-performance acetone gas sensor. Sens Actuator B Chem. 2021;332:129212. https://doi.org/10.1016/j.snb.2020.129212.
[18] Jia XH, Tian MG, Dai RR, Lian DD, Han S, Wu XY, Song HJ. One-pot template-free synthesis and highly ethanol sensing properties of $ZnSnO_3$ hollow microspheres. Sens Actuator B Chem. 2017;240:376. https://doi.org/10.1016/j.snb.2016.08.146.
[19] Yan Y, Liu JY, Zhang HS, Song DL, Li JQ, Yang PP, Zhang ML, Wang J. One-pot synthesis of cubic $ZnSnO_3$/ZnO heterostructure composite and enhanced gas-sensing performance. J Alloys Compd. 2019;780:193. https://doi.org/10.1016/j.jallcom.2018.11.310.
[20] Sasmal A, Medda SK, Devi PS, Sen S. Nano-ZnO decorated $ZnSnO_3$ as efficient fillers in PVDF matrixes: toward simultaneous enhancement of energy storage density and efficiency and improved energy harvesting activity. Nanoscale. 2020;12(40):20908. https://doi.org/10.1039/d0nr02057e.
[21] Yin YY, Shen YB, Zhou PF, Liu R, Li A, Zhao SK, Liu WG, Wei DZ, Wei KF. Fabrication, characterization and n-propanol sensing properties of perovskite-type $ZnSnO_3$ nanospheres based gas sensor. Appl Surf Sci. 2020;509:145335. https://doi.org/10.1016/j.apsusc.2020.145335.
[22] Tuc Altaf C, Coskun O, Kumtepe A, Sankir M, Sankir ND. Bifunctional ZnO nanowire/$ZnSnO_3$ heterojunction thin films for photoelectrochemical water splitting and photodetector applications. Mater Lett. 2022;322:132450. https://doi.org/10.1016/j.matlet.2022.132450.
[23] Baruah S, Dutta J. Zinc stannate nanostructures: hydrothermal synthesis. Sci Technol Adv Mater. 2011;12(1):013004. https://doi.org/10.1088/1468-6996/12/1/013004.
[24] Xu JY, Zhang C. Oxygen vacancy engineering on cerium oxide nanowires for room-temperature linalool detection in rice aging. J Adv Ceram. 2022;11(10):1559. https://doi.org/10.1007/s40145-022-0629-8.
[25] Liang HP, Guo LP, Cao NJ, Hu HY, Li H, de Rooij NF, Umar A, Algarni H, Wang Y, Zhou GF. Practical room temperature formaldehyde sensing based on a combination of visible-light activation and dipole modification. J Mater Chem A. 2021;9(42):23955. https://doi.org/10.1039/d1ta06346d.
[26] Wang ZY, Sackmann A, Gao S, Weimar U, Lu GY, Liu S, Zhang T, Barsan N. Study on highly selective sensing behavior of ppb-level oxidizing gas sensors based on Zn_2SnO_4 nanoparticles immobilized on reduced graphene oxide under humidity conditions. Sens Actuator B Chem. 2019;285:590. https://doi.org/10.1016/j.snb.2019.01.109.
[27] Yu SW, Jia XH, Yang J, Wang SZ, Li Y, Song HJ. Highly sensitive ethanol gas sensor based on CuO/$ZnSnO_3$ heterojunction composites. Mater Lett. 2021;291:129531. https://doi.org/10.1016/j.matlet.2021.129531.
[28] Li Y, Lu YL, Wu KD, Zhang DZ, Debliquy M, Zhang C. Microwave-assisted hydrothermal synthesis of copper oxide--based gas-sensitive nanostructures. Rare Met. 2021;40(6):1477. https://doi.org/10.1007/s12598-020-01557-4.
[29] Li ZS, Liu XH, Zhou M, Zhang SL, Cao SZ, Lei GL, Lou CM, Zhang J. Plasma-induced oxygen vacancies enabled ultrathin ZnO films for highly sensitive detection of triethylamine. J Hazard Mater. 2021;415:125757. https://doi.org/10.1016/j.jhazmat.2021.125757.
[30] Liu JJ, Zhang LY, Cheng B, Fan JJ, Yu JG. A high-response formaldehyde sensor based on fibrous Ag-ZnO/In_2O_3 with multi-level heterojunctions. J Hazard Mater. 2021;413:125352. https://doi.org/10.1016/j.jhazmat.2021.125352.
[31] Gai LY, Lai RP, Dong XH, Wu X, Luan QT, Wang J, Lin HF, Ding WH, Wu GL, Xie WF. Recent advances in ethanol gas sensors based on metal oxide semiconductor heterojunctions. Rare Met. 2022;41(6):1818. https://doi.org/10.1007/s12598-021-01937-4.
[32] Lei GL, Pan HY, Mei HS, Liu XH, Lu GC, Lou CM, Li ZS, Zhang J. Emerging single atom catalysts in gas sensors. Chem Soc Rev. 2022;51(16):7260. https://doi.org/10.1039/d2cs00257d.
[33] Xu YS, Zheng LL, Yang C, Zheng W, Liu XH, Zhang J. Oxygen vacancies enabled porous SnO_2 thin films for highly sensitive detection of triethylamine at room temperature. ACS Appl Mater Interfaces. 2020;12(18):20704. https://doi.org/10.1021/acsami.0c04398.
[34] Shruthi J, Jayababu N, Ghosal P, Reddy MVR. Ultrasensitive sensor based on Y_2O_3-In_2O_3 nanocomposites for the detection of methanol at room temperature. Ceram Int. 2019;45(17):21497. https://doi.org/10.1016/j.ceramint.2019.07.141.
[35] Yuan ZY, Yang F, Zhu HM, Meng FL, Ibrahim M. High-response n-butanol gas sensor based on ZnO/In_2O_3 heterostructure. Rare Met. 2023;42(1):198. https://doi.org/10.1007/s12598-022-02162-3.
[36] Yan M, Wu Y, Hua ZQ, Lu N, Sun WT, Zhang JB, Fan S. Humidity compensation based on power-law response for MOS sensors to VOCs. Sens Actuator B Chem. 2021;334:129601. https://doi.org/10.1016/j.snb.2021.129601.
[37] Jiang LL, Chen ZY, Cui Q, Xu S, Tang FL. Experimental and DFT-D3 study of sensitivity and sensing mechanism of $ZnSnO_3$ nanosheets to C_3H_6O gas. J Mater Sci. 2022;57(5):3231. https://doi.org/10.1007/s10853-021-06855-5.
[38] Yang ZJ, Zou HS, Zhang YY, Liu FM, Wang J, Lv SY, Jiang L, Wang CG, Yan X, Sun P, Zhang LJ, Duan Y, Lu GY. The introduction of defects in $Ti_3C_2T_x$ and $Ti_3C_2T_x$-assisted reduction of graphene oxide for highly selective detection of ppb-level NO_2. Adv Funct Mater. 2022;32(15):2108959. https://doi.org/10.1002/adfm.202108959.
[39] Dong SY, Xia LJ, Chen XY, Cui LF, Zhu W, Lu ZS, Sun JH, Fan MH. Interfacial and electronic band structure optimization for the adsorption and visible-light photocatalytic activity of macroscopic $ZnSnO_3$/graphene aerogel. Compos Part B: Eng. 2021;215:108765. https://doi.org/10.1016/j.compositesb.2021.108765.
[40] Kabitakis V, Gagaoudakis E, Moschogiannaki M, Kiriakidis G, Seitkhan A, Firdaus Y, Faber H, Yengel E, Loganathan K, Deligeorgis G, Tsetseris L, Anthopoulos TD, Binas V. A low--power CuSCN hydrogen sensor operating reversibly at room temperature. Adv Funct Mater. 2022;32:2102635. https://doi.org/10.1016/j.compositesb.2021.108765.

[41] van den Broek J, Abegg S, Pratsinis SE, Guntner AT. Highly selective detection of methanol over ethanol by a handheld gas sensor. Nat Commun. 2019;10:4220. https://doi.org/10.1038/s41467-019-12223-4.
[42] Yao MS, Li WH, Xu G. Metal-organic frameworks and their derivatives for electrically-transduced gas sensors. Coordin Chem Rev. 2021;426:213479. https://doi.org/10.1016/j.ccr.2020.213479.
[43] Chen WY, Jiang XF, Lai SN, Peroulis D, Stanciu L. Nanohybrids of a MXene and transition metal dichalcogenide for selective detection of volatile organic compounds. Nat Commun. 2020;11(1):1302. https://doi.org/10.1038/s41467-020-15092-4.
[44] Zhao X, Li Q, Xu L, Zhang Z, Kang Z, Liao Q, Zhang Y. Interface engineering in 1D ZnO-based heterostructures for photoelectrical devices. Adv Funct Mater. 2022;32(11):2106887. https://doi.org/10.1002/adfm.202106887.
[45] Veeralingam S, Badhulika S. Enhanced carrier separation assisted high-performance piezo-phototronic self-powered photodetector based on core-shell $ZnSnO_3$@In_2O_3 heterojunction. Nano Energy. 2022;98:107354. https://doi.org/10.1016/j.nanoen.2022.107354.
[46] Zhang DZ, Yang ZM, Yu SJ, Mi Q, Pan QN. Diversiform metal oxide-based hybrid nanostructures for gas sensing with versatile prospects. Coord Chem Rev. 2020;413:213272. https://doi.org/10.1016/j.ccr.2020.213272.
[47] Pan QN, Yang ZM, Wang WW, Zhang DZ. Sulfur dioxide gas sensing at room temperature based on tin selenium/tin dioxide hybrid prepared via hydrothermal and surface oxidation treatment. Rare Met. 2021;40(6):1588. https://doi.org/10.1007/s12598-020-01575-2.
[48] Meng JP, Li Z. Schottky-contacted nanowire sensors. Adv Mater. 2020;32(28):2000130. https://doi.org/10.1002/adma.202000130.
[49] Xu JY, Liao HL, Zhang C. $ZnSnO_3$ based gas sensors for pyridine volatile marker detection in rice aging during storage. Food Chem. 2023;408:135204. https://doi.org/10.1016/j.foodchem.2022.135204.